



TECHNICAL ARTICLE

# High-Temperature Sintering Behavior of $\text{Gd}_2\text{O}_3$ - $\text{Yb}_2\text{O}_3$ Co-doped 8YSZ Ceramic for Thermal Barrier Coatings

Haiyuan Yu, Yunyun Shi, Mengchuan Shi, Qian Bian, Zhaolu Xue, and Shihong Zhang

Submitted: 3 August 2022 / Revised: 25 February 2023 / Accepted: 1 March 2023

Multivariate rare-earth co-doped zirconia is one of the candidate materials for ultra-high-temperature thermal barrier coatings.  $\text{GdYb}$ -8YSZ ( $90\text{ZrO}_2$ - $4\text{Y}_2\text{O}_3$ - $3\text{Gd}_2\text{O}_3$ - $3\text{Yb}_2\text{O}_3$ , mol.%) nanopowder and its bulk ceramic were successfully fabricated. Microstructure, thermal conductivity and sintering behavior of  $\text{GdYb}$ -8YSZ ceramic at  $1400^\circ\text{C}$  were investigated. The results showed that  $\text{GdYb}$ -8YSZ nanopowder was composed of a single c- $\text{ZrO}_2$  phase with the particle size in the range of 20–40 nm. The thermal conductivity of  $\text{GdYb}$ -8YSZ does not change much with temperature, in the range of  $1.31$ – $1.74\text{ W m}^{-1}\text{ K}^{-1}$  from room temperature to  $1400^\circ\text{C}$ . This is mainly due to the coupling effect of oxygen vacancy defects, lattice distortion and photon heat conduction. However, the grain size of  $\text{GdYb}$ -8YSZ ceramic gradually increased from  $1.43$  in the as-prepared state to  $3.44\text{ }\mu\text{m}$  after 96 h sintering, and  $\text{GdYb}$ -8YSZ had good high-temperature phase stability and poor sintering resistance at  $1400^\circ\text{C}$ .

**Keywords**  $\text{GdYb}$  co-doped 8YSZ, high-temperature sintering behavior, thermal barrier coating, thermal conductivity

## 1. Introduction

Thermal barrier coatings (TBCs) can provide thermal protection for hot-end components of gas turbine engine, such as heat-insulation, high-temperature oxidation corrosion and gas ablation resistance, and achieve remarkable effectiveness (Ref 1–3). Currently, (6–8 wt.%) yttrium oxide partially stabilized zirconia (8YSZ) is the most successful and widely used TBC ceramic material due to its high fracture toughness, high thermal expansion coefficient, low thermal conductivity and other excellent properties (Ref 2–4). However, with the continuous improvement of thrust–weight ratio and thermal efficiency of the engine, the actual working environment temperature of key components of gas turbine engine is getting higher and higher, which brings great challenges to the safe and stable operation of TBCs and has become one of the urgent problems to be solved. 8YSZ is prone to phase transformation and poor comprehensive performance when it is in service for a long time at above  $1200^\circ\text{C}$ , leading to premature failure and limiting its long-term application (Ref 1, 4–6). Therefore, in

order to deal with the harsh service environment of high-temperature hot-end components, it is extremely urgent to develop a new TBC with low thermal conductivity and good high-temperature phase stability.

Among many candidate materials for TBCs, multi-rare-earth-doped 8YSZ, namely introducing one, two or even multiple rare-earth elements into 8YSZ, is one of the effective ways to improve thermal insulation performance and high-temperature phase stability and is also the research focus of TBCs (Ref 6–10). Fan et al. investigated the high-temperature phase stability, thermal cycling and CMAS corrosion behavior of  $\text{Sc}_2\text{O}_3$ - $\text{Y}_2\text{O}_3$  co-stabilized  $\text{ZrO}_2$  material and TBCs (Ref 8, 9). Layered gradient ScYSZ TBCs exhibited a long thermal cycle life, a low sintering rate and a large strain tolerance due to the presence of vertical cracks and a large amount of unmelted nanoparticles in different layer structures of the thermal barrier coating. The addition of  $\text{Sc}_2\text{O}_3$  to YSZ coating could significantly enhance the corrosion resistance to CMAS because of the low solubility of  $\text{Sc}^{3+}$  in CMAS melt. Wu et al. pointed out  $\text{YO}_{1.5}$ - $\text{TaO}_{2.5}$  co-doped  $\text{ZrO}_2$  as a potential TBC material, which showed significantly enhanced CMAS resistance compared to the traditional 17 mol.%  $\text{YO}_{1.5}$  stabilized  $\text{ZrO}_2$  (17YSZ), and proposed the strategies to improve the CMAS resistance of  $\text{ZrO}_2$ -based TBC materials (Ref 10). Fang et al. reported thermophysical properties of  $\text{Yb}_2\text{O}_3$  and  $\text{Y}_2\text{O}_3$  co-stabilized  $\text{ZrO}_2$  (YbYSZ) and the interaction between YbYSZ and CMAS through experiments and first principles (Ref 11, 12). Compared with traditional YSZ, YbYSZ has better thermophysical properties, and the low mobility rate of  $\text{Yb}^{3+}$  in CMAS melt provides a new method to resist the infiltration and corrosion of CMAS. Wang et al. studied the phase stability and thermophysical properties of  $\text{CeO}_2$  and  $\text{TiO}_2$  co-stabilized  $\text{ZrO}_2$  as a potential TBC (Ref 13). The phase stability, fracture toughness and sintering resistance of  $\text{CeO}_2$  and  $\text{TiO}_2$  co-stabilized  $\text{ZrO}_2$  ceramics decreased with the  $\text{TiO}_2$  content rising.  $(\text{Ce}_{0.15}\text{Ti}_{0.05})\text{Zr}_{0.8}\text{O}_2$  with a single tetragonal phase, low thermal conductivity and the best comprehensive performances, is one of the candidate materials for thermal barrier coatings.  $\text{Gd}_2\text{O}_3$ -

Haiyuan Yu and Yunyun Shi jointly completed the experiment and wrote the draft of this paper.

**Haiyuan Yu**, Beijing Beiyue Functional Materials Corporation, Beijing 100192, China; **Yunyun Shi**, **Mengchuan Shi**, **Zhaolu Xue**, and **Shihong Zhang**, Key Laboratory of Green Fabrication and Surface Technology of Advanced Metal Materials, Anhui University of Technology, Ministry of Education, Maanshan 243002, China; **Qian Bian**, Modern Analysis and Testing Center, Anhui University of Technology, Maanshan 243002, China. Contact e-mail: zhaoluxue@163.com.

Yb<sub>2</sub>O<sub>3</sub> co-doped YSZ (GdYb-YSZ) ceramic material with high melting point, good corrosion resistance, high-temperature phase stability and low thermal conductivity is an ideal TBC ceramic material (Ref 6, 14–16). Gao et al. studied the effect of Gd<sub>2</sub>O<sub>3</sub> on the phase composition, fracture toughness and thermal conductivity of Gd<sub>2</sub>O<sub>3</sub>-Yb<sub>2</sub>O<sub>3</sub>-Y<sub>2</sub>O<sub>3</sub>-ZrO<sub>2</sub> (GYYZO) ceramics (Ref 17). The GYYZO ceramic with 15 wt.% Gd<sub>2</sub>O<sub>3</sub> has the highest hardness, elastic modulus and fracture toughness, and the lowest thermal conductivity. Bahamirian et al. reported the microstructure and cyclic oxidation properties of plasma-sprayed YSZ/GYYZO nanostructured TBCs at 1100 °C (Ref 18). It was found that the GYYZO coating formed a bimodal microstructure composed of columnar grains and nanoparticles left over from the original nanopowder, and the introduction of YSZ intermediate transition layer greatly improved the high-temperature oxidation resistance. Although the phase composition, mechanical and thermophysical properties of Gd<sub>2</sub>O<sub>3</sub>-Yb<sub>2</sub>O<sub>3</sub> co-doped 8YSZ ceramic material and its coating have been widely studied and reported, the high-temperature sintering behavior of Gd<sub>2</sub>O<sub>3</sub>-Yb<sub>2</sub>O<sub>3</sub> co-doped 8YSZ ceramic material and its coating has been rarely reported.

GdYb-8YSZ (90ZrO<sub>2</sub>-4Y<sub>2</sub>O<sub>3</sub>-3Gd<sub>2</sub>O<sub>3</sub>-3Yb<sub>2</sub>O<sub>3</sub>, mol.%) is composed of Gd, Yb and Y rare-earth atoms replacing Zr lattice positions in ZrO<sub>2</sub> lattice, making it a cubic crystal structure. (Crystal cell structure diagram is shown in Fig. 1.) In this paper, GdYb-8YSZ nanopowder was prepared by chemical coprecipitation method, and the ceramic block material was prepared. The phase composition, mechanical properties and thermal conductivity of GdYb-8YSZ ceramic were studied. Finally, the sintering behavior of GdYb-8YSZ ceramic block material at 1400 °C was discussed in detail.

## 2. Experimental

In this experiment, Zr(NO<sub>3</sub>)<sub>4</sub>·5H<sub>2</sub>O, Y(NO<sub>3</sub>)<sub>3</sub>·6H<sub>2</sub>O, Yb(NO<sub>3</sub>)<sub>3</sub>·5H<sub>2</sub>O, Gd(NO<sub>3</sub>)<sub>3</sub>·6H<sub>2</sub>O (all purity ≥ 99.99%, from Jining Zhongkai New Materials Co., LTD.) were used to prepare GdYb-8YSZ nanopowder. The GdYb-8YSZ nanopowder was placed in a ball mill with ethanol as dispersant, and ground in the ball mill for 10 h at a speed of 360 r/min, and

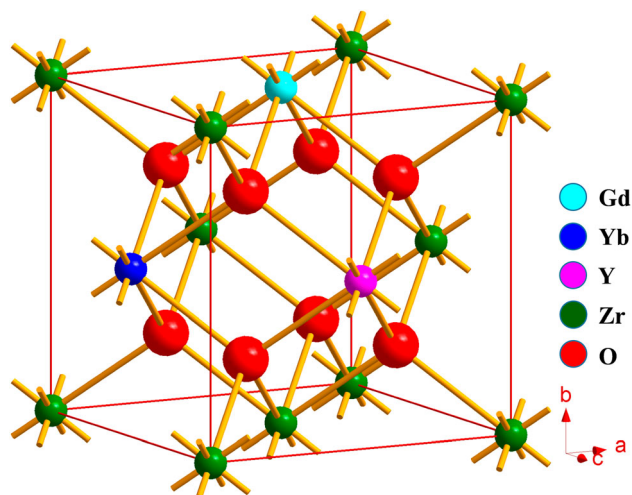


**Fig. 1** Schematic diagram of GdYb co-doped 8YSZ crystal cell structure

then taken out to dry. The GdYb-8YSZ nanopowder slurry after ball-milling was dried in an electric blast drying oven at 50 °C for 10 h until all the anhydrous ethanol evaporated. The oven is always closed in the drying process, so as to avoid a large amount of air into the oven and cause a fire. Subsequently, the dried powder was placed in a mold with a diameter of 15 mm and dry-pressed on the YLJ-20TA electric tablet press (Shenyang Kejing Auto-instrument Co., LTD) for 30 s with a pressure of 15 MPa to get the GdYb-YSZ ceramic green billet. Finally, the ceramic green billet was placed in a high-temperature sintering furnace at 1450 °C for 4 h to obtain GdYb-8YSZ block ceramic.

X-ray diffractometer (XRD, Rigaku Ultima IV, Japan) was used to characterize the phase composition of the sample (Cu target, scanning angle of 10–90°, scanning speed of 10°/min). Phase composition of the sample was further confirmed by Renishaw inVia Raman Microscope, and the test conditions were consistent with literature (Ref 3, 19). The morphology and size of GdYb-8YSZ nanopowder were characterized through the JEOL-JEM 2100 high-resolution transmission electron microscope (HR-TEM). Scanning electron microscopy (SEM, Phenom XL, Netherlands) was used to detect the microstructure of samples. In addition, the indentation parameters of fracture toughness were measured by SEM photographs. The porosity of the sample can be calculated by referring to the literature (Ref 20). The thermal diffusivity ( $\alpha$ ) of ceramics from room temperature to 1400 °C was measured by NETZSCH LFA 427 HT HyperFlash laser heat conductor (German) with 12.7 mm diameter and 1 mm thickness. The specific heat capacity of GdYb-8YSZ was measured by the NETZSCH STA 449F3 thermal analyzer equipment. The block ceramic is coated with a thin layer of graphite before testing. The elastic modulus of the sample was measured by nanoindentation instrument (Agilent G200, USA). (The indentation depth was 600 nm, and the load retention time was 10 s.) MH-5LD microhardness tester was used to test the microhardness of samples (1000 gf, 30 s), 10 different test points were selected to avoid accidental error, and the average value was calculated as the final Vickers hardness. The fracture toughness was calculated from the Vickers hardness indentation according to Eq 1, where  $H$  is the microhardness (GPa),  $a$  is 1/2 of the diagonal length, and  $c$  is the length from the Vickers indentation center to the crack end. The method of calculating fracture toughness was consistent with studies (Ref 20, 21). In this case, the hardness tester load was 10 N, and hold time was 30 s,

$$K_{IC} = 0.16 H a^{1/2} (c/a)^{-3/2} \quad (\text{Eq 1})$$

## 3. Results and Discussion

### 3.1 Microstructure and Thermal Conductivity

Figure 2 shows the TEM morphology and XRD patterns of GdYb-8YSZ powder. According to the TEM image (Fig. 2a) of the powder, the particle size of the powder is concentrated in the range of 20–40 nm, reaching the nanometer level, which provides a basis for the preparation of GdYb-8YSZ nanostructured thermal barrier coating. It can be seen from Fig. 2b that GdYb-8YSZ powder is mainly composed of c-ZrO<sub>2</sub> phase. Compared with the diffraction peak of the standard c-ZrO<sub>2</sub> crystal phase (JCPDF#81-1550), the XRD diffraction peak of

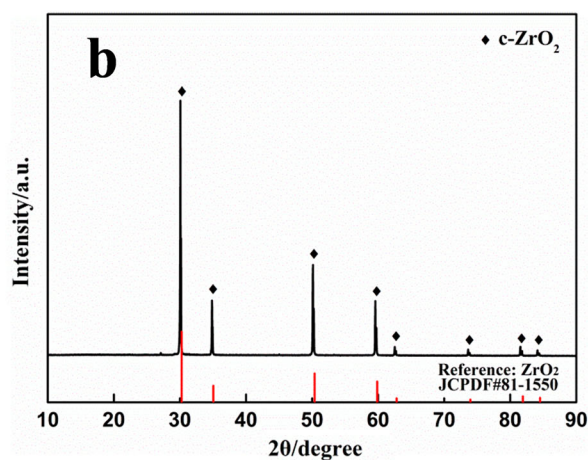
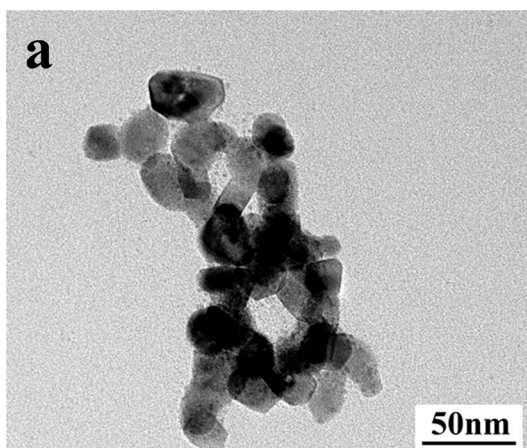


**Fig. 2** TEM image (a) and XRD patterns (b) of GdYb co-doped 8YSZ nanopowder

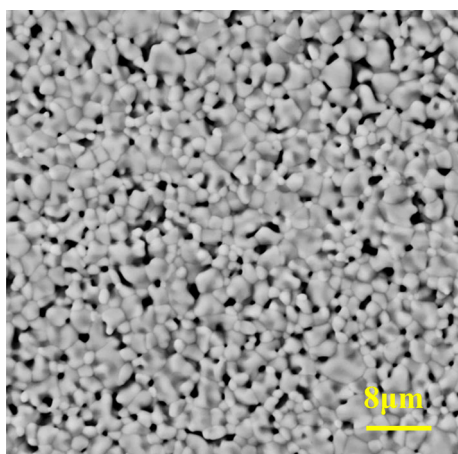


**Fig. 3** Surface morphology of GdYb-8YSZ ceramic after sintering at 1450 °C for 4 h

the powder shifts to a smaller angle as a whole, because the radius of  $\text{Gd}^{3+}$  and  $\text{Yb}^{3+}$  is larger than that of  $\text{Zr}^{4+}$ , and the lattice constant becomes larger in the process of replacing the latter. This result also indicates that  $\text{Gd}^{3+}$  and  $\text{Yb}^{3+}$  ions effectively replace  $\text{Zr}^{4+}$  ions.

Figure 3 presents the surface image of GdYb-8YSZ block ceramic sintered at 1450 °C for 4 h. The grain of GdYb-8YSZ ceramic is irregular and polygonal, but the size is not uniform and there are micropores (as shown in Fig. 3). In addition, there are clear grain boundaries between the grains, indicating that there are no unreacted oxides and other second phases between the grains.

According to the specific heat capacities of  $\text{Gd}_2\text{O}_3$ ,  $\text{Y}_2\text{O}_3$ ,  $\text{Yb}_2\text{O}_3$  and  $\text{ZrO}_2$  compounds and the Neumann–Kopp rule (Ref 22), the specific heat capacities of GdYb-8YSZ ceramic between room temperature and 1400 °C were calculated. The measured and calculated specific heat capacity values of GdYb-8YSZ are shown in Fig. 4. The specific heat capacity of GdYb-8YSZ generally increases with the temperature rising. The difference is that the measured specific heat capacity fluctuates in a small range of 0.448–0.493  $\text{J g}^{-1} \text{K}^{-1}$  at the below 1000 °C, while the theoretical calculated value increases in a small range of 0.429–0.59  $\text{J g}^{-1} \text{K}^{-1}$ . The specific heat capac-

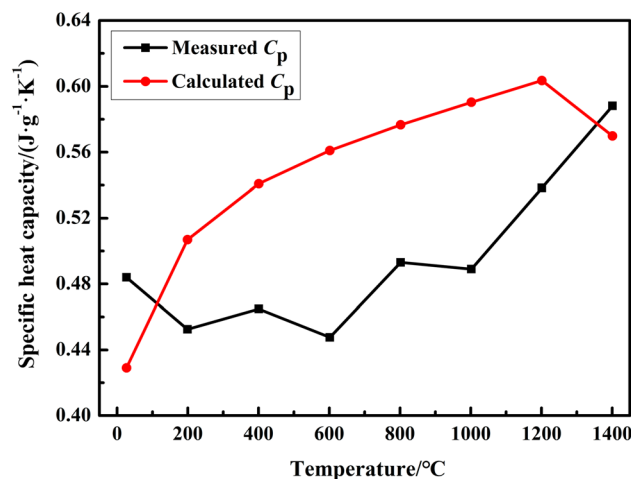


**Fig. 4** Variation of the measured and calculated specific heat capacity values of GdYb-8YSZ ceramic with temperature

ity fluctuates from 0.448 to 0.604  $\text{J g}^{-1} \text{K}^{-1}$  between room temperature and 1400 °C, but the range of change of specific heat capacity values is relatively small in the whole temperature range.

The thermal conductivity ( $\lambda$ ) of the sample is calculated from density ( $\rho$ ), specific heat capacity ( $C_p$ ) and thermal diffusivity ( $\alpha$ ) based on  $\lambda = \rho \cdot \alpha \cdot C_p$  (Ref 19). Figure 5 exhibits the corresponding relationship between thermal diffusivity, thermal conductivity and temperatures of GdYb-8YSZ ceramic. The thermal diffusivity of GdYb-8YSZ ceramic ranges from 0.478 to 0.627  $\text{mm}^2/\text{s}$  in the range of room temperature to 1400 °C, as shown in Fig. 5a. The thermal diffusivity is inversely proportional to the test temperature; that is, the thermal diffusivity decreases with the increase in temperature. This is because phonon conduction plays a crucial role in heat conduction in most inorganic nonmetallic materials (Ref 23, 24). The higher the temperature is, the stronger the phonon scattering and the lower thermal diffusivity will be. As can be seen from Fig. 5b, the measured and calculated thermal conductivity of GdYb-8YSZ varies little with temperature. The thermal conductivity varies from 1.31 to 1.74  $\text{W m}^{-1} \text{K}^{-1}$  from room temperature to 1400 °C. The calculated and measured thermal conductivities differ only from 0 to



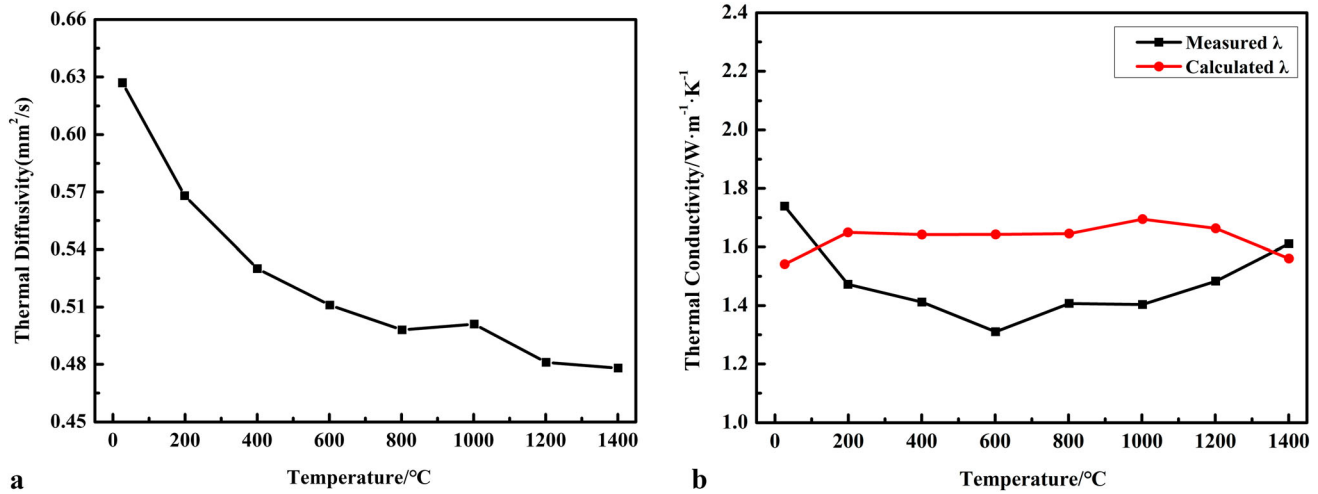


**Fig. 5** Variation of thermal diffusivity (a) and the measured and calculated thermal conductivity (b) of GdYb-8YSZ ceramic with temperature

$0.3 \text{ W m}^{-1} \text{ K}^{-1}$  in the test temperature range. The measured thermal conductivity of GdYb-8YSZ at  $1000^\circ\text{C}$  is  $1.403 \text{ W m}^{-1} \text{ K}^{-1}$ , which is about 30% lower than that of 8YSZ at the same temperature reported in the literature (Ref 6). From the above XRD test results (Fig. 2), it can be deduced that GdYb co-doping results in lattice distortion. Originally, there are a certain number of oxygen vacancies in the 8YSZ lattice, and the substitution of two rare-earth ions ( $\text{Gd}^{3+}$  and  $\text{Yb}^{3+}$ ) with different masses and ionic radii produces more oxygen vacancies. Both lattice distortion and oxygen vacancy will enhance phonon scattering, resulting in a decrease in thermal conductivity. However, with the increase in temperature, the role of heat conduction of photons is gradually enhanced, resulting in an increase in thermal conductivity, which can be obviously observed in the measured thermal conductivity values. The coupling effect of oxygen vacancy defects, lattice distortion and photon heat conduction results in little change of GdYb-8YSZ ceramic within the test temperature range.

### 3.2 High-temperature Sintering Behavior

In order to achieve long life and high reliability of aero-engine, TBCs is bound to be exposed to high-temperature service environment for a long time, which poses a severe challenge to the stability of microstructure and performance of TBCs under long-term high temperature (Ref 1, 25). Therefore, the sintering resistance of TBC ceramic material is particularly important. In order to further explore the sintering resistance of GdYb-8YSZ ceramic, GdYb-8YSZ was sintered at  $1400^\circ\text{C}$  for 24 h, 48 h, 72 h and 96 h, respectively. Figure 6 shows the surface morphology of GdYb-8YSZ ceramic sintered at  $1400^\circ\text{C}$  for different times. It can be found that the grain boundary is relatively clear and no other phase is generated at the grain boundary during the whole sintering process. However, as a whole, the grain size gradually increases with the extension of sintering time, the number of surface pores gradually decreases, and the density of ceramics also rises. The reason for this phenomenon is that high temperature increases the driving force of oxygen vacancy migration, and long sintering time accelerates the growth of grain, resulting in denser ceramics.

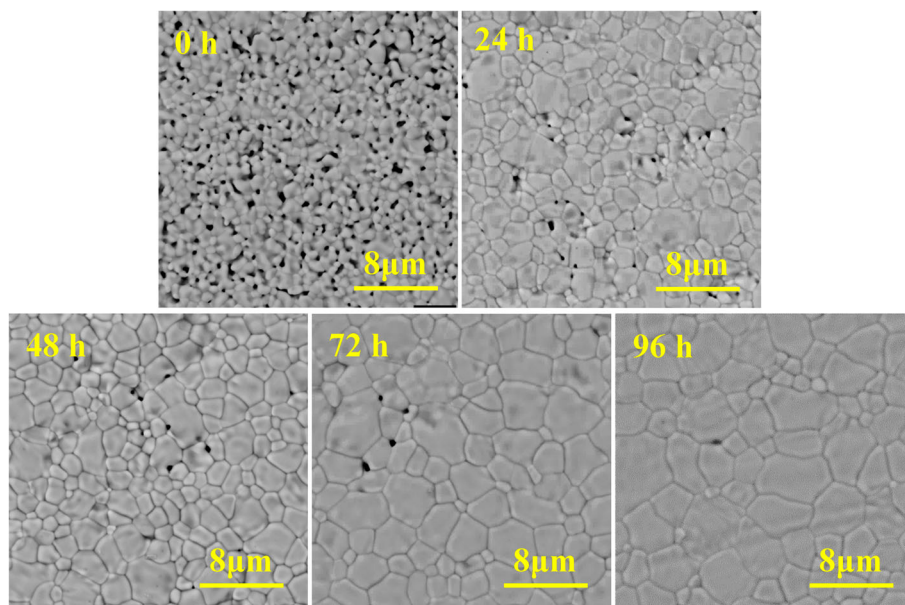
Ten surface backscattered electron images with 9000 times magnification were randomly collected from each sample for image analysis, and the average particle size of the sample was determined by rectangular procedure (Ref 21). According to Eq 2, the average grain size in a single image can be calculated, and the final grain size is taken as the average size of ten images:

$$D = \sqrt{\frac{4A}{\pi(n_1 + n_0/2)}} \quad (\text{Eq 2})$$

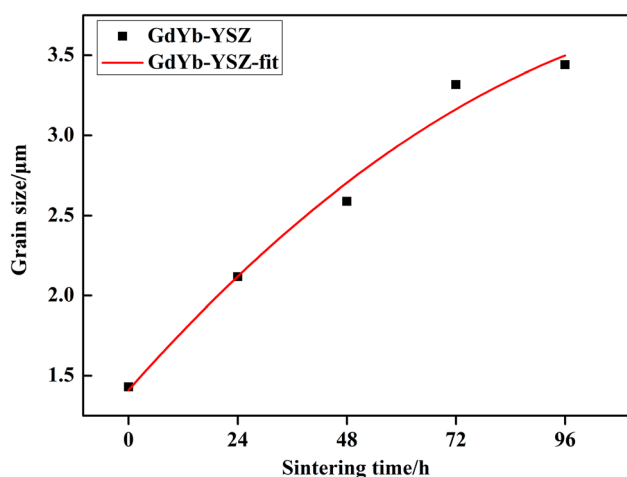
where  $A$  is the area of the rectangle, and  $n_1$  and  $n_0$  are the number of grains inside the rectangle and on the boundary of the rectangle, respectively.

Figure 7 shows the average grain size of GdYb-8YSZ ceramic sintered at  $1400^\circ\text{C}$  as a function of sintering time. It can be seen that the grain size gradually increases with the extension of sintering time at  $1400^\circ\text{C}$ , from  $1.43 \mu\text{m}$  in the as-prepared state to  $3.44 \mu\text{m}$  after 96 h sintering. On the whole, the grain growth is more obvious, indicating that Gd and Yb co-doped 8YSZ ceramic has poor sintering resistance. However, the change curve of average grain size with sintering time also reflects that the growth rate of average grain size gradually decreases with the extension of sintering time. The average porosities of the GdYb-8YSZ ceramic sintered at  $1400^\circ\text{C}$  for 0, 24, 48, 72 and 96 h were 9.27, 6.63, 4.67, 3.93 and 3.1%, respectively.

In order to test the phase stability of ceramic materials at high temperature, the XRD patterns of GdYb-8YSZ ceramic at different sintering times were analyzed, and their XRD patterns are shown in Fig. 8a. GdYb-8YSZ ceramic is composed of a single c- $\text{ZrO}_2$  without phase transition, and no new phase is formed before and after sintering. In addition, Fig. 8b presents the Raman spectra of GdYb-8YSZ ceramic at different sintering times.  $\text{ZrO}_2$  has three different crystal phases: monoclinic, tetragonal and cubic. According to studies (Ref 26, 27), Raman spectra are more sensitive to tetragonal and monoclinic phases in  $\text{ZrO}_2$ . Raman vibration peak at about  $630 \text{ cm}^{-1}$  (Fig. 8b) belongs to the characteristic peak of c- $\text{ZrO}_2$  cubic phase, and no other characteristic peaks exist, indicating that the sintering time has no significant effect on the phase composition of GdYb-8YSZ ceramic. All these proved that



**Fig. 6** Surface morphology of GdYb-8YSZ ceramic sintered at 1400 °C for different times



**Fig. 7** Average grain size of GdYb-8YSZ ceramic with sintering time

GdYb-8YSZ had excellent high-temperature phase stability at 1400 °C.

To study the sintering behavior of GdYb-8YSZ ceramics at high temperature, it is necessary to elucidate the change of microstructure and mechanical properties of GdYb-8YSZ ceramics with sintering time. The schematic of indentation and cracks of GdYb-8YSZ ceramics before and after sintering for 96 h at 1400 °C are shown in Fig. 9. According to the length of indent and crack, the fracture toughness of GdYb-8YSZ ceramic before and after sintering for 96 h was calculated by Eq 1. Similarly, the fracture toughness values of GdYb-8YSZ ceramic at 1400 °C for different sintering times can be also calculated. Figure 10 shows the hardness and fracture toughness of GdYb-8YSZ ceramic sintered at 1400 °C for different times. Vickers hardness of GdYb-8YSZ ceramic is positively proportional to the sintering time. This is because the as-prepared GdYb-8YSZ ceramic has higher porosity, leading to its lower hardness. With the extension of sintering time, part of the pores are closed, resulting in the increase in density and

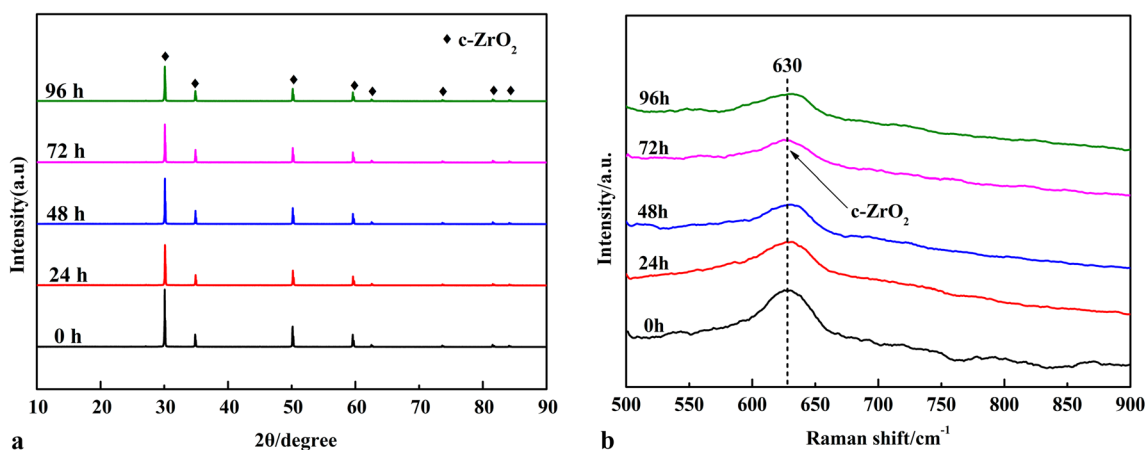


**Fig. 8** XRD patterns (a) and Raman spectra (b) of GdYb-8YSZ ceramic sintered at 1400 °C for different times

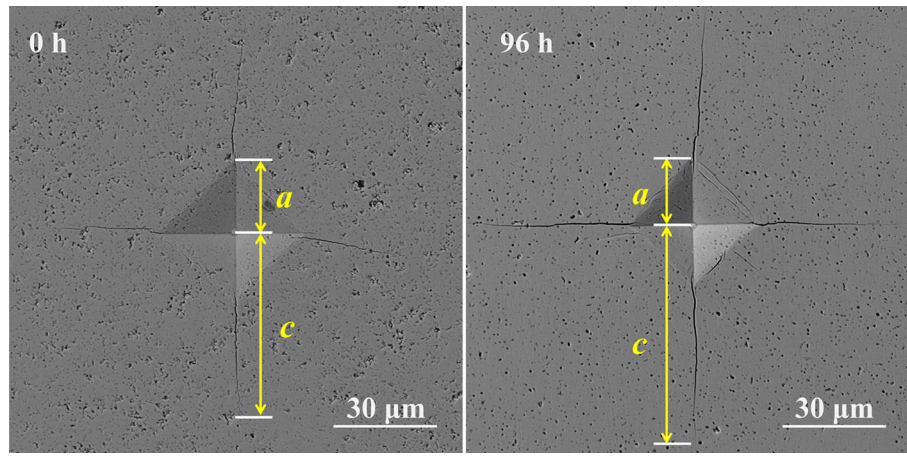


**Fig. 9** Schematic of indentation and cracks of GdYb-8YSZ ceramics before and after sintering for 96 h at 1400 °C

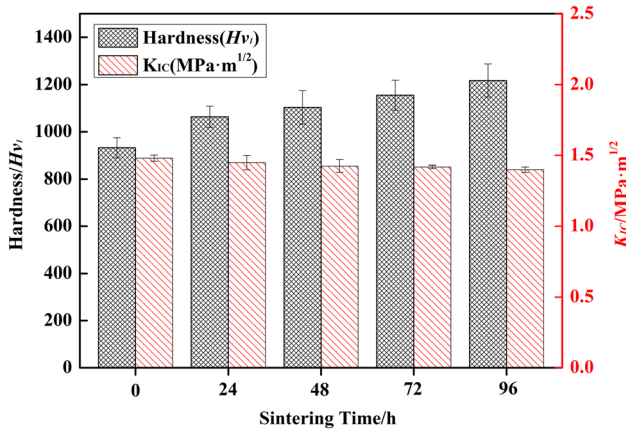


**Fig. 10** The hardness and fracture toughness of GdYb-8YSZ ceramic sintered at 1400 °C for different times

hardness. In the hot-cold alternating high-temperature environment, it is generally hoped that ceramic materials/coatings have large fracture toughness, so as to improve the thermal cycling performance of TBCs (Ref 28). Therefore, the influence

of long-term high-temperature sintering on the fracture toughness of ceramic materials is also of great significance. The existence of the pore will hinder the crack propagation during the fracture process, which makes the material more resistant to crack propagation. Some pores are closed in the process of sintering, so the fracture toughness of ceramic materials will be reduced. But the fracture toughness ( $K_{IC}$ ) is mainly determined by the binding energy of crystal lattice, to a certain extent, associated with the lattice deformation and crystal disorder (Ref 28). The phase composition and crystal structure of GdYb-8YSZ ceramic did not change (as shown in Fig. 8a), so the fracture toughness value decreased but changed little during the sintering process, suggesting that the sintering time had little influence on the fracture toughness of GdYb-8YSZ ceramic.

Figure 11 shows the elastic modulus and load-displacement curves of nanoindentation of GdYb-8YSZ ceramic sintered at 1400 °C for different times. Generally speaking, elastic modulus of ceramic material increases with the decrease in porosity. The ceramic materials are gradually densified in the sintering process (as shown in Fig. 7), so the elastic modulus should increase. But most of the elastic modulus of materials is determined by the composition and crystal structure of itself (Ref 29). With the increase in sintering time at 1400 °C, the

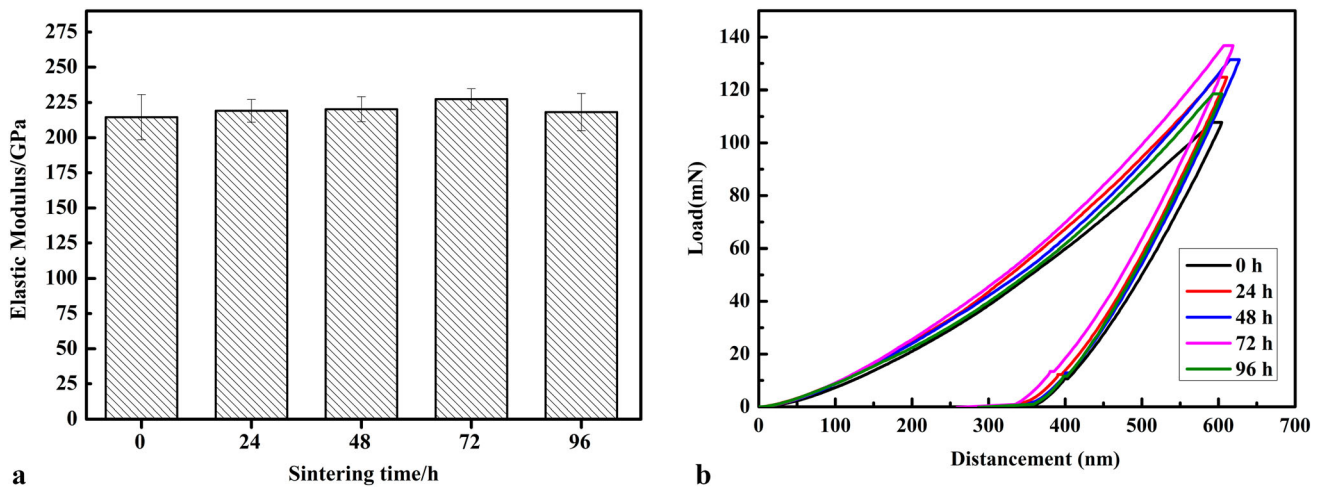


**Fig. 11** Elastic modulus (a) and load-displacement curves of nanoindentation (b) of GdYb-8YSZ ceramic sintered at 1400 °C for different times



composition and phase structure of GdYb-8YSZ ceramics do not change, resulting in little change in elastic modulus after sintering. Meanwhile, it can be seen from the load–displacement curves of nanoindentation of GdYb-8YSZ ceramic at different sintering times (Fig. 11b) that the variation trend of elastic modulus is basically the same as that of other mechanical properties (such as hardness and fracture toughness).

## 4. Conclusion

- (1) GdYb-8YSZ nanopowder was composed of a single c-ZrO<sub>2</sub> phase. The particle size of the nanometer powders was between 20 and 40 nm.
- (2) The thermal conductivity of GdYb-8YSZ does not change much with temperature, in the range of 1.31–1.74 W m<sup>−1</sup> K<sup>−1</sup> from room temperature to 1400 °C. This is mainly due to the coupling effect of oxygen vacancy defects, lattice distortion and photon heat conduction.
- (3) The phase composition of GdYb-8YSZ ceramic does not change with the increase in sintering time at 1400 °C, indicating that GdYb-8YSZ has good high-temperature phase stability. However, the grain size of GdYb-8YSZ gradually increases from 1.43 μm in the as-prepared state to 3.44 μm after 96 h sintering, suggesting that GdYb co-doped ZrO<sub>2</sub> ceramic has poor sintering resistance at 1400 °C. At the same time, the hardness of GdYb-8YSZ ceramic slightly increases with the increase in sintering time. However, the fracture toughness and elastic modulus hardly change.

## Acknowledgment

This work was supported by Natural Science Foundation of Universities of Anhui Province (RZ2100003743), Natural Science Foundation of Anhui Province (Grant No. 1908085QE219), Key Laboratory of Green Fabrication and Surface Technology of Advanced Metal Materials (GFST2022ZR04) and Postgraduate Science Research Project of Anhui Province (YJS20210337).

## References

1. R. Darolia, Thermal Barrier Coatings Technology: Critical Review, Progress Update, Remaining Challenges and Prospects, *Int. Mater. Rev.*, 2013, **58**(6), p 315–348
2. E. Bakan and R. Vaßen, Ceramic Top Coats of Plasma-Sprayed Thermal Barrier Coatings: Materials, Processes, and Properties, *J. Therm. Spray Technol.*, 2017, **26**(12), p 992–1010
3. Z. Xue, Y. Zhu, H. Yu, M. Shi, X. Liu, and S. Zhang, Nano-agglomerated Powder and Thermal Shock Cycling Property of 8YSZ Nano-structured Thermal Barrier Coating, *Surf. Coat. Tech.*, 2022, **433**, p 128173
4. G. Li and G. Yang, Understanding of Degradation-Resistant Behavior of Nanostructured Thermal Barrier Coatings with Bimodal Structure, *J. Mater. Sci. Technol.*, 2019, **35**(3), p 231–238
5. L. Guo, H. Xin, Z. Zhang, X. Zhang, and F. Ye, Microstructure Modification of Y<sub>2</sub>O<sub>3</sub> Stabilized ZrO<sub>2</sub> Thermal Barrier Coatings by Laser Glazing and the Effects on the Hot Corrosion Resistance, *J. Adv. Ceram.*, 2020, **9**(2), p 232–242
6. R. Vaßen, M.O. Jarligo, T. Steinke, D.E. Mack, and D. Stöver, Overview on Advanced Thermal Barrier Coatings, *Surf. Coat. Tech.*, 2010, **205**(4), p 938–942
7. E.V. Dudnik, S.N. Lakiza, I.N. Hrechanyuk, A.K. Ruban, V.P. Redko, I.O. Marek, V.B. Shmibelsky, A.A. Makudera, and N.I. Hrechanyuk, Thermal Barrier Coatings Based on ZrO<sub>2</sub> Solid Solutions, *Powder Metall. Met. C+*, 2020, **59**(3), p 179–200
8. W. Fan, Y. Bai, Y. Wang, T. He, Y. Gao, Y. Zhang, X. Zhong, B. Li, Z. Chang, and Y. Ma, Microstructural Design and Thermal Cycling Performance of a Novel Layer-Gradient Nanostructured Sc<sub>2</sub>O<sub>3</sub>-Y<sub>2</sub>O<sub>3</sub> co-Stabilized ZrO<sub>2</sub> Thermal Barrier Coating, *J. Alloy. Compd.*, 2020, **829**, p 154525
9. W. Fan, Y. Bai, Y. Liu, Y. Kang, Y. Wang, Z. Wang, and W. Tao, Corrosion Behavior of Sc<sub>2</sub>O<sub>3</sub>-Y<sub>2</sub>O<sub>3</sub> Co-stabilized ZrO<sub>2</sub> Thermal Barrier Coatings with CMAS Attack, *Ceram. Int.*, 2019, **45**(12), p 15763–15767
10. D. Wu, Y. Yao, X. Shan, F. Yang, X. Zhao, and P. Xiao, Equimolar YO<sub>1.5</sub> and TaO<sub>2.5</sub> Co-doped ZrO<sub>2</sub> as a Potential CMAS-Resistant Material for Thermal Barrier Coatings, *J. Am. Ceram. Soc.*, 2021, **104**(2), p 1132–1145
11. H. Fang, W. Wang, S. Deng, T. Yang, H. Zhu, J. Huang, D. Ye, and X. Guo, Interaction Between Yb<sub>2</sub>O<sub>3</sub>-Y<sub>2</sub>O<sub>3</sub> Co-stabilized ZrO<sub>2</sub> Ceramic Powder and Molten Silicate Deposition, and Its Implication on Thermal Barrier Coating Application, *Mater. Charact.*, 2021, **180**, p 111418
12. H. Fang, W. Wang, J. Huang, Y. Li, and D. Ye, Corrosion Behavior and Thermo-Physical Properties of a Promising Yb<sub>2</sub>O<sub>3</sub> and Y<sub>2</sub>O<sub>3</sub> Co-stabilized ZrO<sub>2</sub> Ceramic for Thermal Barrier Coatings Subject to Calcium-Magnesium-Aluminum-Silicate (CMAS) Deposition: Experiments and First-Principles Calculation, *Corros. Sci.*, 2021, **182**, p 109230
13. J. Wang, J. Sun, Q. Jing, B. Liu, H. Zhang, Y. Yu, J. Yuan, S. Dong, X. Zhou, and X. Cao, Phase Stability and Thermo-Physical Properties of ZrO<sub>2</sub>-CeO<sub>2</sub>-TiO<sub>2</sub> Ceramics For Thermal Barrier Coatings, *J. Eur. Ceram. Soc.*, 2018, **38**(7), p 2841–2850
14. L. Guo, C. Zhang, M. Li, W. Sun, Z. Zhang, and F. Ye, Hot Corrosion Evaluation of Gd<sub>2</sub>O<sub>3</sub>-Yb<sub>2</sub>O<sub>3</sub> Co-doped Y<sub>2</sub>O<sub>3</sub> Stabilized ZrO<sub>2</sub> Thermal Barrier Oxides Exposed to Na<sub>2</sub>SO<sub>4</sub>+V<sub>2</sub>O<sub>5</sub> Molten Salt, *Ceram. Int.*, 2017, **43**(2), p 2780–2785
15. K. Bobzin, L. Zhao, M. Öte et al., A Highly Porous Thermal Barrier Coating Based on Gd<sub>2</sub>O<sub>3</sub>-Yb<sub>2</sub>O<sub>3</sub> Co-doped YSZ, *Surf. Coat. Tech.*, 2019, **366**, p 349–354
16. Y. Zhang, L. Guo, Y. Yang, H. Guo, H. Zhang, and S. Gong, Influence of Gd<sub>2</sub>O<sub>3</sub> and Yb<sub>2</sub>O<sub>3</sub> Co-doping on Phase Stability, Thermo-Physical Properties and Sintering of 8YSZ, *Chin. J. Aeronaut.*, 2012, **25**(6), p 948–953
17. P. Gao, S. Zeng, C. Jin, B. Zhang, B. Chen, Z. Yang, Y. Guo, M. Liang, J. Li, Q. Li, Y. Lu, L. Jia, and D. Zhao, Effect of Gd<sub>2</sub>O<sub>3</sub> Addition on the Microstructure and Properties of Gd<sub>2</sub>O<sub>3</sub>-Yb<sub>2</sub>O<sub>3</sub>-Y<sub>2</sub>O<sub>3</sub>-ZrO<sub>2</sub> (GYYZO) Ceramics, *Materials*, 2021, **14**(23), p 7470
18. M. Bahamirian, S. Hadavi, M. Farvizi, A. Keyvani, and M. Rahimpour, Microstructure and cyclic oxidation of yttria-stabilized zirconia/nanostructured ZrO<sub>2</sub>-9.5Y<sub>2</sub>O<sub>3</sub>-5.6Yb<sub>2</sub>O<sub>3</sub>-5.2Gd<sub>2</sub>O<sub>3</sub> thermal barrier coating at 1373 K, *J. Mater. Eng. Perform.*, 2020, **29**(11), p 7080–7093
19. M. Shi, Z. Xue, Z. Zhang, X. Ji, E. Byon, and S. Zhang, Effect of spraying powder characteristics on mechanical and thermal shock properties of plasma-sprayed YSZ thermal barrier coating, *Surf. Coat. Tech.*, 2020, **395**, p 125913
20. X. Wang, Z. Xue, Z. Zhou, E. Byon, and S. Zhang, Influence of Yb<sub>2</sub>Si<sub>2</sub>O<sub>7</sub> Doping Concentration on Mechanical Properties and Thermal Conductivity of Yb<sub>2</sub>Si<sub>2</sub>O<sub>7</sub>-Yb<sub>2</sub>Si<sub>2</sub>O<sub>7</sub> Composite Ceramics, *J. Alloy. Compd.*, 2022, **889**, p 161718
21. Y. Guo, W. He, and H. Guo, Thermo-Physical and Mechanical Properties of Yb<sub>2</sub>O<sub>3</sub> and Sc<sub>2</sub>O<sub>3</sub> Co-doped Gd<sub>2</sub>Zr<sub>2</sub>O<sub>7</sub> Ceramics, *Ceram. Int.*, 2020, **46**(11), p 18888–18894
22. Y. Liang, Y. Che, and X. Liu, *Manual of Practical Inorganic Matter Thermodynamics*, Northeastern University Press, Shenyang, 1993
23. H. Lu, C. Wang, C. Zhang, and S. Tong, Thermo-Physical Properties of Rare-Earth Hexaaluminates LnMgAl<sub>11</sub>O<sub>19</sub> (Ln: La, Pr, Nd, Sm, Eu and Gd) Magnetoplumbite for Advanced Thermal Barrier Coatings, *J. Eur. Ceram. Soc.*, 2015, **35**, p 1297–1306

24. Z. Qu, T. Sparks, W. Pan, and D. Clarke, Thermal Conductivity of the Gadolinium Calcium Silicate Apatites: Effect of Different Point Defect Types, *Acta Mater.*, 2011, **59**(10), p 3841–3850
25. G. Li, L. Wang, and G. Yang, Achieving Self-enhanced Thermal Barrier Performance Through a Novel Hybrid-Layered Coating Design, *Mater. Design*, 2019, **167**, p 107647
26. X. Ren and W. Pan, Mechanical Properties of High-temperature-degraded Ytria-Stabilized Zirconia, *Acta Mater.*, 2014, **69**, p 397–406
27. C. Perry, D. Liu, and P. Robert, Phase Characterization of Partially Stabilized Zirconia by Raman Spectroscopy, *J. Am. Ceram. Soc.*, 1985, **68**(8), p 184–187
28. L. Guo, Y. Zhang, X. Zhao, C. Wang, and F. Ye, Thermal expansion and fracture toughness of  $(\text{RE}_{0.9}\text{Sc}_{0.1})_2\text{Zr}_2\text{O}_7$  (RE= La, Sm, Dy, Er) ceramics, *Ceram. Int.*, 2016, **42**(1), p 583–588
29. C. Wan, Z. Qu, A. Du, and W. Pan, Influence of B Site Substituent Ti on the Structure and Thermophysical Properties of  $\text{A}_2\text{B}_2\text{O}_7$ -Type Pyrochlore  $\text{Gd}_2\text{Zr}_2\text{O}_7$ , *Acta Mater.*, 2009, **57**(16), p 4782–4789

**Publisher's Note** Springer Nature remains neutral with regard to jurisdictional claims in published maps and institutional affiliations.

Springer Nature or its licensor (e.g. a society or other partner) holds exclusive rights to this article under a publishing agreement with the author(s) or other rightsholder(s); author self-archiving of the accepted manuscript version of this article is solely governed by the terms of such publishing agreement and applicable law.